Journal of Physics D: Applied Physics

Non-destructive imaging for quality assurance of MRAM junctions

To cite this article before publication: Edward Jackson *et al* 2019 *J. Phys. D: Appl. Phys.* in press https://doi.org/10.1088/1361-6463/ab47b6

Non-Destructive Imaging for quality assurance of MRAM junctions

E. Jackson,[1)] Y. Wu,[1)] W. Frost,[1)] J.-Y. Kim,[2),a)] M. Samiepour,[1)] K. Elphick,[1)] M. Sun,[3)] T. Kubota,[3),4)] K. Takanashi, [3),4),5)] T. Ichimose,[5),6)] S. Mizukami [4),5),6)] and A. Hirohata [1),*]

[1)] *Department of Electronic Engineering, University of York, York YO10 5DD, United Kingdom*

[2)] *Department of Physics, University of York, York YO10 5DD, United Kingdom*

[3)] *Institute for Materials Research, Tohoku University, Sendai 980-8577, Japan*

[4)] *Center for Spintronics Research Network, Tohoku University, Sendai 980-8577, Japan*

[5)] *Center for Science and Innovation in Spintronics, Core Research Cluster, Tohoku University, Sendai 980-8577, Japan*

[6)] *WPI Advanced Institute for Materials Research, Tohoku University, Sendai 980-8577, Japan*

[a)] Present address: *Institute of Physics, Johannes Gutenberg University Mainz, Mainz 55128, Germany*

* Corresponding author, E-mail: atsufumi.hirohata@york.ac.uk

Abstract

We have developed a new non-destructive sub-surface interfacial imaging technique. By controlling the penetration depth of the incident electrons, through control of the electron beam acceleration voltage in a scanning electron microscope, we can observe sub-surface interfaces. The voltages for imaging are selected based on Monte Carlo electron flight simulations, where the two voltages have >5% difference between the number of backscattered electrons generated in the layers above and below the buried interface under investigation. Due to the non-destructive nature, this imaging method can be used alongside an applied electrical current and voltage, allowing concurrent observations of the interfacial structures and transport properties, *e.g.*, effective and active junction area, to occur. Magnetic tunnel junctions used in magnetic random access memory have been imaged and the data has been fed back to improve their fabrication processes. Our imaging method is therefore highly useful as both a quality assurance and development tool for magnetic memory and nanoelectronic devices.

1. Introduction

The development of MRAM is progressing well [1],with several examples of industrial use [2]. Increasing the yield of these devices is an important step towards full uptake. MRAM studies also show that the quality of the interfaces, particularly around the tunnel barrier, influence devices performance. Whilst device performance can be tested readily using many electrical probe techniques, such as the four-terminal method, these techniques provide little information on the root cause of this performance difference. This means that to both increase yield and assist development more analysis techniques are required.

There are a multitude of microanalytic techniques available, briefly represented in Fig. 1(a). The primary method to investigate devices and their interfaces is cross-sectional transmission electron microscopy (TEM) [3]. TEM relies on a destructive preparation process to remove and thin a lamella from a device or wafer. Whilst this provides atomically resolved data, the timely preparation process makes it impractical for large scale studies and quality assurance (QA), relying on representative samples instead. The destructive preparation also reduces the flexibility of the investigative direction, but more importantly causes doubt over the source of any features that are absent or present. It is impossible to determine whether any defects were introduced during the thinning process itself.

For the reasons discussed above it is important to find a new way of studying interfaces in devices at a similar resolution non-destructively. A method utilising a scanning electron microscope (SEM) has been proposed [4]. This method controls the penetration depth of backscattered electrons by varying the energy of the beam using the acceleration voltage and an applied bias voltage. An example of this using a permalloy-copper interface is visualized in Fig. 1(b). Subtractive imaging then provides subsurface and interfacial information in a non-destructive manner. Incidentally the information is taken from a top down point of view, which is suited for mapping large areas or multiple samples on wafers. As it is non-destructive, and requires little preparation, it easily fits into QA processes as a device characterisation technique.

This technique utilises the simulation of electron propagation through solids to inform or predict the ideal operating acceleration voltages to use for a subtraction which bounds the interface or region of interest. Once these voltages have been found images are taken at an appropriate, but matching, magnification. Finally these images are subtracted using bespoke software, which accounts for both the positional misalignment and any difference in contrast between the images.

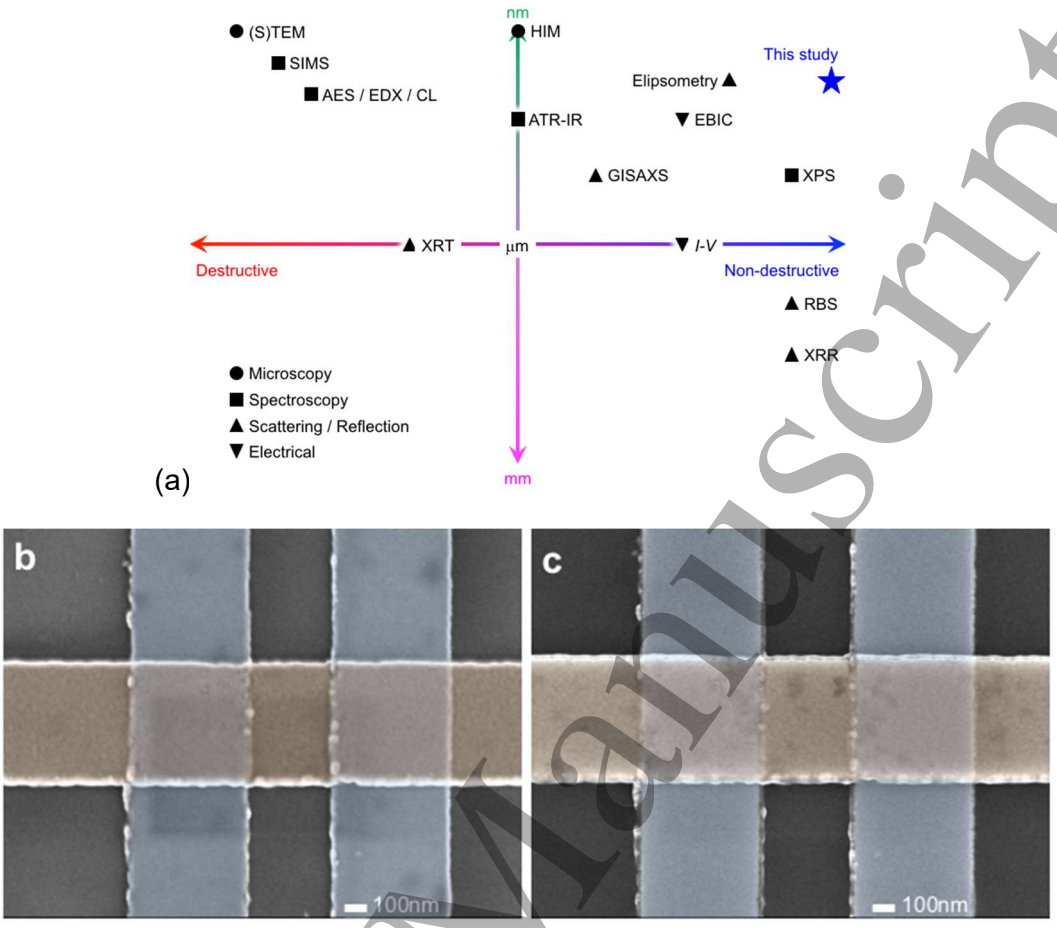

Fig. 1 (a) Evaluation techniques for embedded junctions. SEM images taken at the electron-beam acceleration of (b) 1 and (c) 5 keV. Originally published in: [5].

2. Imaging Process

2.1. SEM Image Acquisition

Whilst the use of an SEM is considered trivial it is important to understand fully the base equipment on which this technique has been developed. This section will briefly cover the processes and underlying physics required to generate and direct an electron beam towards a sample in an SEM. It will then cover the products and their detection [6].

The electrons in an SEM are liberated from a source. Once released these electrons are accelerated towards the sample in a beam using a simple high voltage field, sometimes known as high tension. To direct and narrow the beam of electrons an SEM has several different electromagnetic lenses within it. There are the condenser lenses, the objective lens and the scanning coils. Within the SEM the condenser lenses and objective lenses are controlled simultaneously to demagnify the beam to the required spot size [7]. The condenser lenses are simple electromagnetic lenses, arranged along

the beams flight. The objective lens in the system used for this study (JEOL, JSM 7800F Prime) is a snorkel lens [8]. It extends the field onto the sample, greatly reducing lens abberations when compared with other lens designs.

As well as having a more intricate geometry to allow for probe focusing, the objective lens also contains the stigmators. Stigmators are used to correct a large number of distortions [9]. The objective lens in an SEM also has to house the scanning coils. These are two pairs of small coils housed in or above the objective lens, which apply an electric potential to deflect the beam. This allows the probe to be rastered across the surface, with the first set of coils bending the beam away from the optical axis and the second set bending it back at the desired crossover point.

For the sake of SEM imaging only two products are of any concern, backscattered electrons (BSEs) and secondary electrons (SEs). By definition SEs are electrons that escape the sample with <50 eV and BSEs are any with >50 eV. BSEs are expected to have undergone a handful of interactions within the sample, meaning it probes deep into the sample whilst maintaining good atomic number based contrast. SEs will have undergone many more interactions or have been produced with low energy in the top 5~20 nm of the sample, meaning they provide little contrast, but significant surface information. The SEs are also strongly influenced by the magnetic field of the immersion lens, whilst the BSEs are not. Given this knowledge, the use of energy filters and an appropriately placed detector can provide information on the sample's surface or the elements that make it up.

2.2 Electron Flight Simulation

Electron flight simulations have been used as they provide an opportunity to test multiple ideas or quantify configurations quickly, providing usable and physically applicable statistics. When a model that closely reflects a physical system is used simulations are also able to probe it in a way that is difficult to replicate in experimental studies. Monte Carlo methods have been chosen in this study as they allow an investigation of phenomena with statistically relevant data using powerful single particle models. In this way simulations have not only been used to provide further evidence for its viability, but also to configure and calibrate the depth information received. In this study Monte Carlo simulation of electron trajectory in solids (CASINO) [10] is the program of choice, although other programs with similar methodologies were also utilised to confirm the findings. CASINO has been specifically designed to simulate the operation of SEMs, particularly at low beam energies (<5 keV) [11].

The model for elastic scattering used in CASINO is an empirical model based on the

Mott cross section formula. This provides an elastic scattering cross section close to experimental data. An approximation of the frequency of events occurring is also needed [12] to predict how an electron travels through a solid. This frequency is characterised by the mean free path and is denoted λ_{el}, measured in cm. This represents the average distance an electron travels between elastic scattering events and is given by:

$$\lambda_{el} = \frac{A}{\sigma_{el} N_0 \rho} \quad (1)$$

where σ_{el} is the elastic scattering cross section, A is the atomic weight, N_0 is Avogadro's number and ρ is the volumetric density.

The model for inelastic scattering used in CASINO was proposed by Joy and Luo [13]. They proposed a semi-empirical model which goes beyond Bethe's original model [14] to account for the reducing average energy loss per event once the electron energy is below 10 keV, given by:

$$\frac{dE}{ds} = -7.85 \times 10^4 \frac{Z\rho}{AE_e} \ln\left(\frac{1.166(E_e + kJ)}{J}\right), \quad (2)$$

where dE is the average energy loss through all inelastic interactions, ds is the distance travelled, Z is the atomic number, ρ is the volumetric density, A is the atomic weight, E_e is the electron energy, k is the element specific variable that is fitted empirically with the form $k = 0.7 + 0.07 \log_{10} Z$, and J is the average energy loss per event.

Using Equations (1) and (2) in a Monte Carlo simulation, such as in CASINO, the interaction volume can be visualized. As the interaction volume is a predictor of the actual resolution of SEM it is important to understand how the interaction volume is influenced. Assuming a smooth surface the three dominant effects are the beam energy, sample composition and the angle of incidence of the beam. The substrate thickness can also play a major role when it is <1 μm, but this is not a common in SEM use as the sample substrate is usually much thicker. For the case of a pure sample the composition term depends on Z. For alloys or compounds a combination of Z values are required.

The incident beam energy has a strong effect on the interaction volume. This is shown in Fig. 2 using CASINO to calculate the electron-solid interactions at different incident energies. These simulations are the result of 2,000 electron paths, a low number chosen to generate a clear example. Equation (2) can be used to find the rate at which an electron loses energy. As the rate and energy have an inverse relationship, if E_e is large then the electron travels much further before being spent. The cross-section of electron scattering varies by $1/{E_e}^2$. This means that as E_e increases elastic interactions are initially less likely to happen. When combined with the fact that it also takes longer for

the electron to lose energy this results in a much greater penetration of the sample and more lateral movement as well.

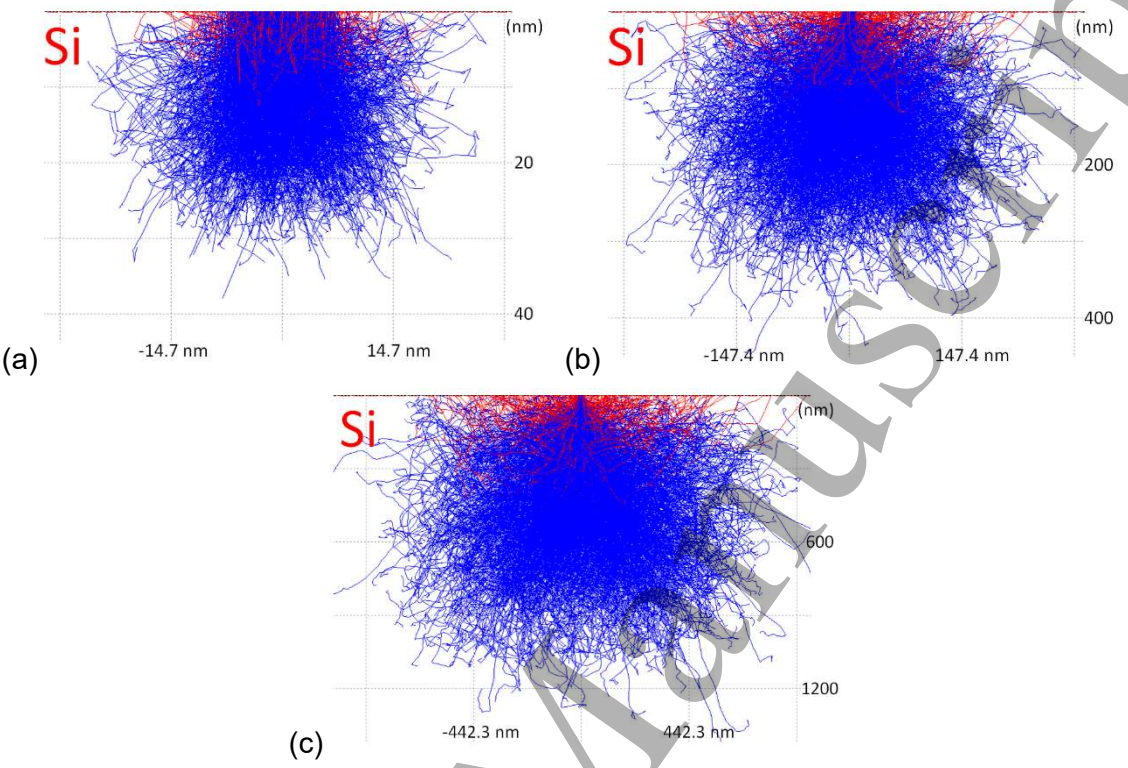

Fig. 2 Demonstration of the effect of changing beam energy, E_e, on the maximum penetration depth of BSEs and spent electrons, simulated in CASINO. (a) 1, (b) 5 and (c) 10 keV.

In a similar manner electron scattering cross-section can be analysed with regards to the atomic number, Z. This shows that electron scattering cross-section varies with Z^2, the opposite correlation to E_e As can be seen in Fig. 3, the interaction volume decreases as Z increases. Once again this figure is produced in CASINO using 2,000 simulated electrons. This occurs because an increase in Z results in a larger Coulomb force. This leads to an increase in the number of scattering events. Not only are these scattering events more frequent, they are also more likely to create a higher angle deflection. This deviates the electrons from their original path more quickly, ejecting them from the sample as BSEs more readily.

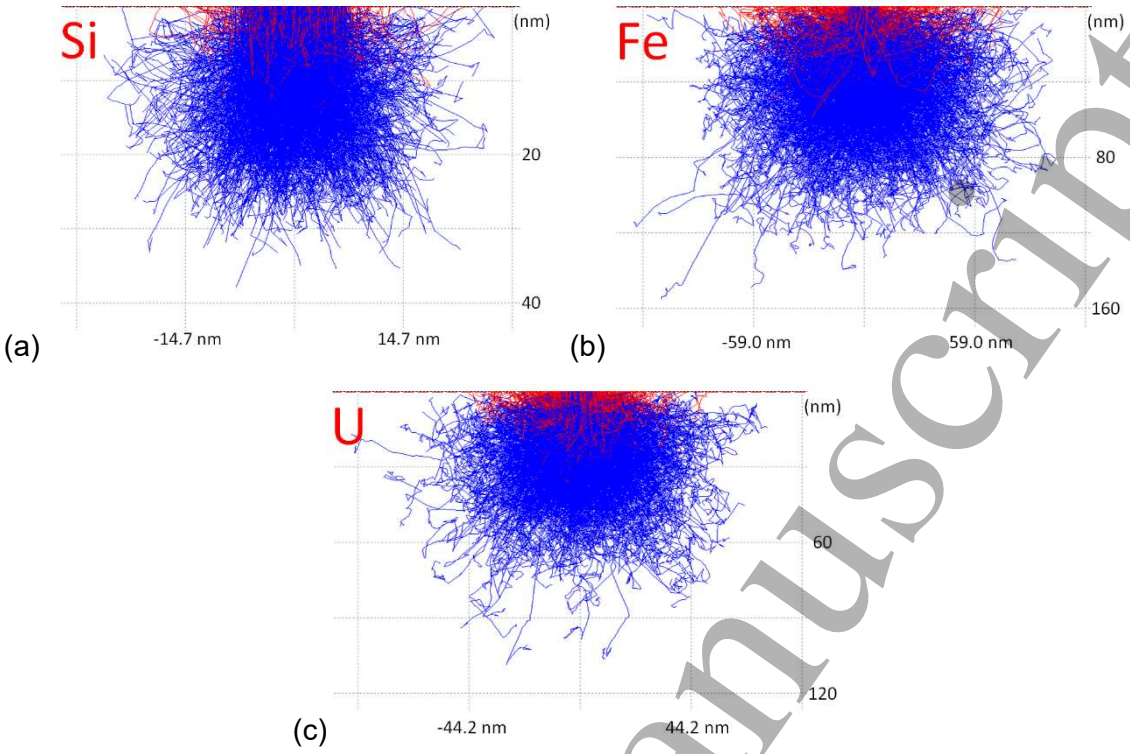

Fig. 3 Demonstration of the effect of changing atomic number, Z, on the maximum penetration depth of BSEs and spent electrons, simulated in CASINO. For each case Z is (a) 14 (Silicon), (b) 26 (Iron) and (c) 92 (Uranium).

The effects of the angle of incidence, θ, are a little less obvious to deduce from the scattering equations. As θ increases the penetration depth is reduced and the interaction volume becomes less symmetric. The electron paths of 2,000 electrons are simulated in CASINO, shown in Fig. 4 to aid the explanation of this occurrence. The most probable change in angle after an elastic collision is ~4º. Given an incident beam perpendicular to the surface as shown in Fig. 3(a), electrons tend to penetrate more deeply into the sample after their initial scattering event. Some electrons experience much larger angles of scattering and be ejected from the sample, however, they are in the minority.

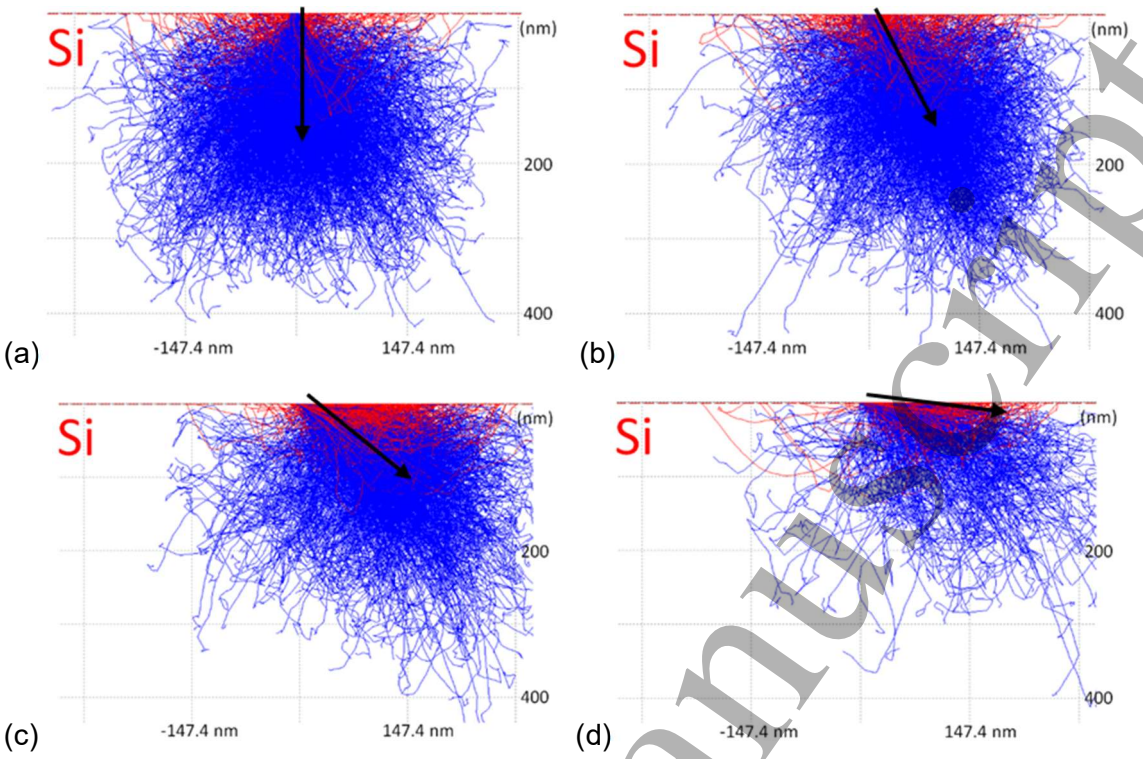

Fig. 4 Demonstration of the effect of changing angle of incidence, θ, on the maximum penetration depth of BSEs and spent electrons, simulated in CASINO. For each case θ is (a) 0, (b) 30, (c) 60 and (d) 89º. These angles are indicated by the arrows on the diagram.

As θ increases scattering will tend to happen either laterally or penetratively as shown in Fig. 4(b). Even at this small angle an asymmetry is created, where electrons are scattering more favourably to the right of the sample. This small angle also reduces the penetration depth by ~15%. It is also worth noting that there is an increase of ~10% in the number of electrons escaping the surface to the right of the incident beam and the corresponding reduction to the left. This is due to the initial scattering events pushing around half of the electrons closer to the surface than in the normal case. Once θ is sufficiently large, such as the case in Figs. 4(c) and (d), a significant distortion of the previously symmetric interaction volume is observed. A reduction of >50% of the penetration depth is also observed. This is due to an exaggeration of the favouring of the scattering direction as described. Kanaya and Okayama proposed that the maximum penetration depth changes approximately with tilt by a factor of $\cos\theta$ [15].

The interaction volume is the cause of the reduction in expected resolution in SEM, however, it also provides significant subsurface information. When performing any study it is important to consider the effects of E_e, Z and θ as they heavily influence the

detected image. This is even more important in heterogeneous samples, such as multilayer structures, as interaction products from subsurface layers are detected and reduce the clarity of information from the surface.

2.3. Image Analysis

This technique requires the direct comparison of two very similar images, taken using an SEM at different beam energies. Once stored in a digital format several steps are required to accomplish this. These steps are: crop image; readjust the contrast; align and transform the image; then perform the comparative action. To accomplish this a semi-automated program was coded in the MATLAB environment.

As previously discussed the technique utilises a controlled penetration depth to probe sub-surface features. As the only information on the depth penetrated is probability data from Monte Carlo simulations using CASINO it is better to image across a series of beam energies, and equivalent penetration depths, to allow for a more thorough comparison. This is particularly important when unpredicted geometric effects need to be accounted for.

As the analysis is just as experimental as the method care has been taken to ensure the results are both repeatable and relevant. Particular care is taken to ensure sufficient simulations are performed, to approximate the penetration depth for each beam energy, with each sample. When dubious or interesting results appear, they should be retested then investigated using other more well recognised techniques. Once corroborated these interesting results became the basis of the work documented.

3. Results and Discussion

3.1. Imaging magnetic tunnel junctions to improve their yield

Once the methodology for the non-destructive imaging technique had been streamlined, the technique was used to investigate batch productions of magnetic tunnel junction (MTJ) devices [16]. This was done with the intent on investigating the interfaces to explain the root cause of low tunneling magnetoresistance (TMR) devices and offer a solution to increase the yield of high TMR devices.

A multilayer wafer, consisting of Cr (80)/Pd (5)/$Co_2Fe_{0.4}Mn_{0.6}Si$ (5 or 30)/MgO (2)/$Co_{0.5}Fe_{0.5}$ (5)/$IrMn_3$ (10)/Ru (7) (thickness in nm), was sputtered onto an MgO(001) substrate. This structure was then etched into a series of MTJ pillars with dimensions ranging between 10x10 and 50x50 μm using both photolithography and Ar-ion milling. The resist used, AZ5214E, was then removed using N-methylpyrrolidone. The milled regions were then filled with Al-O and finally a top electrode of Au (80) was deposited.

Once the MTJs had been formed and isolated, they were electronically tested using a four-terminal methodology. This allowed the devices to be grouped into low (<20%) TMR and high (>80%) TMR devices.

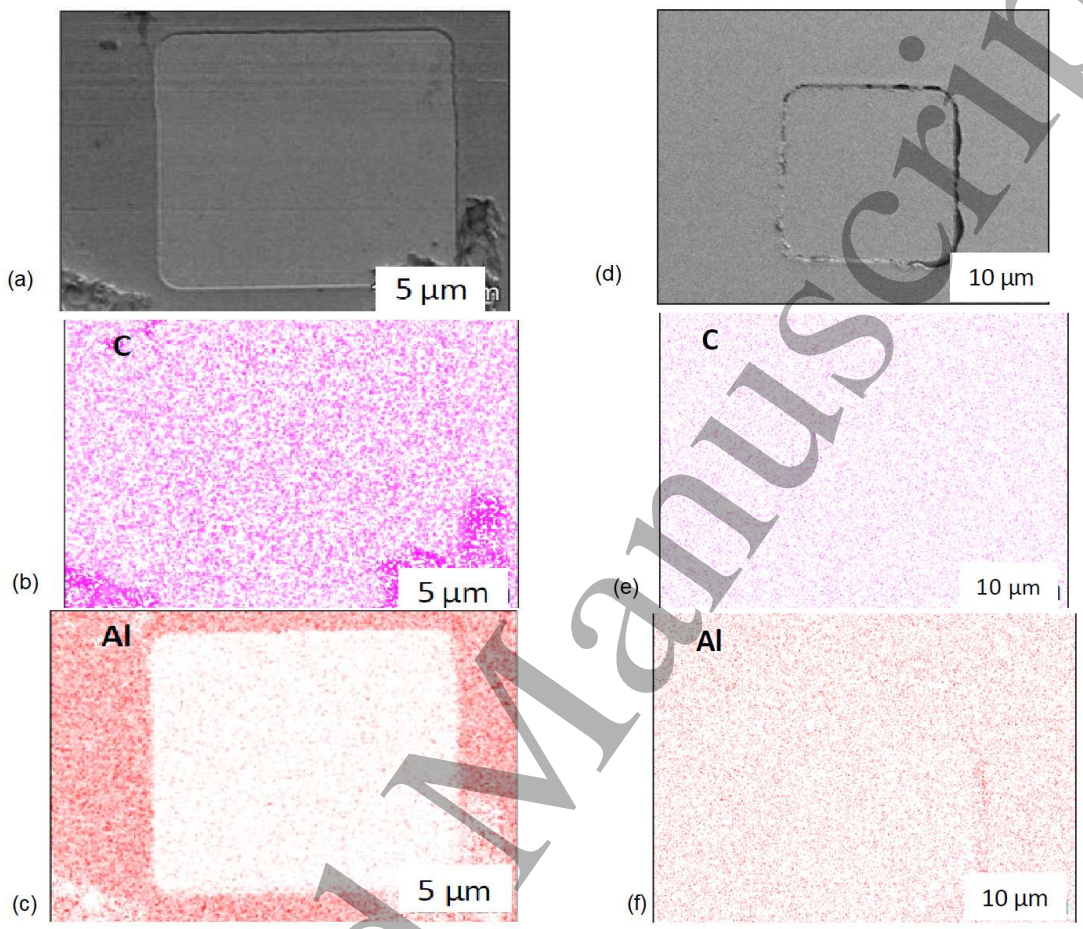

Fig. 5 (a) and (d) are scanning electron images of a high and low TMR junction respectively, taken at 10.5 keV. (b) and (c) are elemental maps of the high TMR device. (e) and (f) are elemental maps of the low TMR device. Originally published in: [16].

Once the devices had been simulated using CASINO, imaging was performed on both high and low TMR MTJs to allow a direct comparison. Figures 5(a) and (d) show a high and low TMR junction respectively. The subtractive imaging highlighted two features; that both MTJs had featureless interfaces and that the edges were drastically different between the two sets of samples. This led to the understanding that the interfacial layers weren't the primary issue in this case, it was something to do with the edges of the structure.

To attempt to identify the root cause of this issue energy dispersive X-ray spectroscopy (EDX) was employed. This allowed the chemical composition of the devices to be probed without needing to change the setup. A typical set of results has been shown in Fig. 5, where (b) and (c) are from the high TMR MTJ and (e) and (f) are from the low TMR MTJ. This analysis showed that there were large discrepancies in the distribution of both Al and C. The low TMR MTJs showed large concentrations in areas at the edge of the structure. This lead to the conclusion that at some point during the deposition of Al-O, the Al is reacting with the C from the resist. This is forming a conductive aluminium carbide along the edge of the MTJ, providing a low resistance path for charge to flow, shunting it and reducing the TMR greatly.

To both test this theory and improve the yield of these devices, a strategy to reduce the likelihood of this carbide formation was put forth. As the energy required for the formation of aluminium carbides is moderately high, a reduction in the deposition energy was chosen as the best course and test. This would increase the deposition time, which could cause other issues in the fabrication process, such as resist hardening. Once the second batch of devices were produced an increase in yield of 15% was recorded. This demonstrated the power of using a mixed technique investigative process, including the non-destructive imaging technique, to identify production faults and improve the yield of complex devices such as MTJs.

The non-destructive imaging technique has also been used to analyse CoFeB-based MTJ devices similarly fabricated. Conventional MTJ wafers were prepared using ultrahigh vacuum magnetron sputtering with the device consisting of Si (substrate)/Ta (5)/Ru (10)/Ta (5)/CoFeB (10)/MgO (2)/CoFeB (2)/Ta (3)/Ru (5)/Ti (20)/Au (280) (thickness in nm). These were then etched into devices. With the non-destructive imaging, details about the quality of the bottom CoFeB/MgO and top MgO/CoFeB interfaces can be obtained without destroying the devices. This allows further testing to be done if required.

(a) 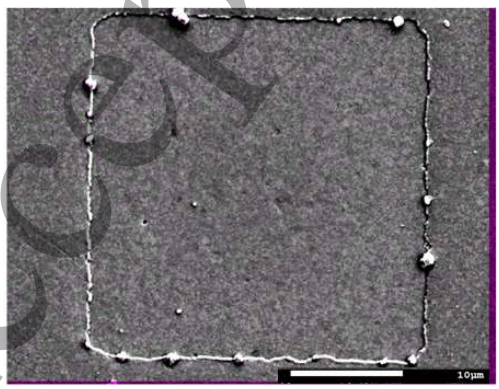 (b) 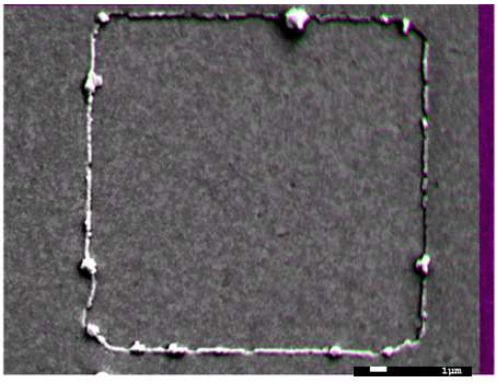

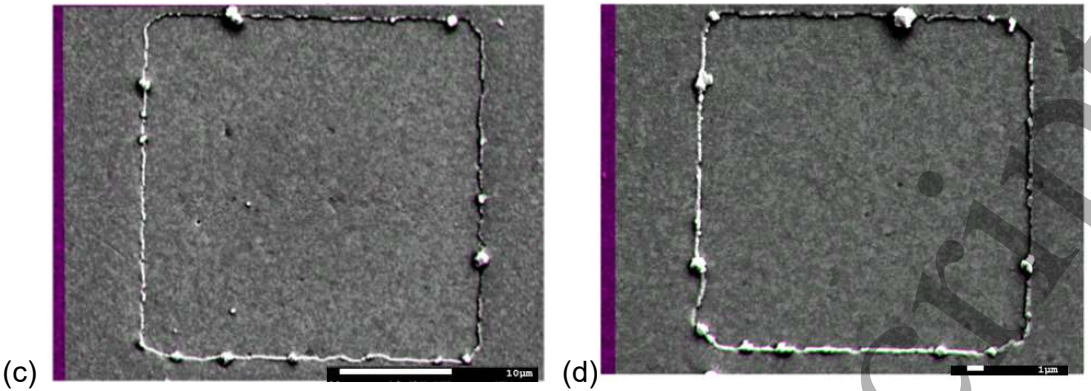

Figure 6 Subtracted SEM images focused on the bottom CoFeB/MgO interfaces for (a) high and (b) low TMR MTJs. The corresponding SEM images on the top MgO/interfaces for (c) high and (d) low TMR MTJs.

CASINO simulations were carried out to determine the suitable acceleration voltages to obtain information from the barrier interface. The imaging voltage subtraction between 16.6 and 16.4 keV as well as 16.4 and 16.2 keV was used to analyse the bottom and top barrier interfaces, respectively. The voltages required are significantly higher than usual as the Au capping layer is very substantial. Two distinctive groups of MTJs were analysed for comparison. Those with a high TMR ratio above 60%, and those with a low TMR ratio below 1.8%, similar to the previous MTJ study. Figure 6 shows the resultant subtraction SEM images using the non-destructive method with the voltages discussed. Figures 6(a) and (c) show the bottom and top barrier interfaces respectively for a high TMR MTJ, whilst Figures 6(b) and (d) show these interfaces for a low TMR MTJ. Black dots in the middle represent observed pinholes and the white dots are contaminants with a high cross-section of electron scattering. Here, the high TMR MTJs are found to contain more contaminants than the low TMR MTJs, whilst having a similar number of pinhole features. These results suggest that during the annealing at 500ºC some contaminants are introduced, either through intermixing or some other process, at the boundaries between layers and grains. These highly scattering contaminants seem to be linked to the increase in TMR ratio. An investigation into the origin of these contaminants is under progress. Using this non-destructive methodology we have managed to quickly supplement the electronic information we have already gathered from the devices. This extra information can be tested and fed back into the production process to optimize procedures and increase the yield.

3.2. Developing CoFe:N as an alternative to CoFe

The non-destructive sub-surface imaging method has also been applied to analyse thin film samples with a ferromagnetic nitride layer. Ferromagnetic CoFe:N has been studied previously as a potential replacement of te conventional ferromagnetic layer, CoFe. The structure of the thin film sample that was investigated was Si (substrate)/Ta (5)/Ru (10)/$Co_{0.75}Fe_{0.25}$:N (15)/Ta (5) (thickness in nanometer). Ta was sputtered on the Si substrate to create an amorphous seed layer for Ru growth. Nitrogen gas was introduced to the chamber at 0.2 Pa pressure during the sputtering of $Co_{0.75}Fe_{0.25}$ at 250ºC. The sample was capped using Ta to prevent oxidation.

Using this structure, a series of simulations were run in CASINO to identify the best beam energies to probe the regions of interest. These simulations identified that a subtraction between 0.6 and 0.7 keV would probe the CoFe:N/Ta interface. They also identified that a subtraction between 2 and 2.2 keV would probe the Ru/CoFe:N interface.

Figure 7(a) is the subtracted image between the SEM images obtained at 0.6 and 0.7 keV. The bloom-like areas where the colour changes from magenta to green indicates that there are defects or vacancies, with a diameter between 3 to 8μm, at the CoFe:N/Ta interface. Figure 7(b) is another subtracted SEM image probing the Ru/CoFe:N interface. Here the bloom-like areas are less prominent than in Fig. 7(a), but still present. These images suggest that there is some sort of sparsely dispersed grain structure, forming initially at the Ru/CoFe:N interface and being overly pronounced at the CoFe:N/Ta interface. The increased pronunciation is likely due to the formation of TaN at granular areas where N has a higher concentration. These formations are less pronounced at the Ru interface as this layer has crystallised before the introduction of N. Reducing the partial pressure of N during the sputtering process could act to reduce the build up of nitrogen outside of the CoFe:N layer, and ensure even distribution, improving the interface quality.

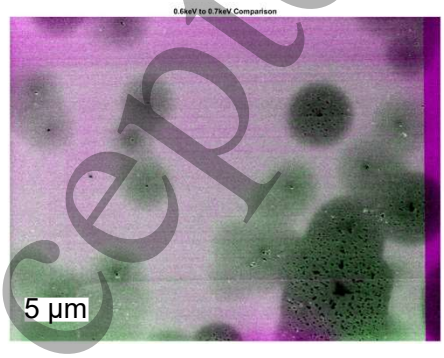

(a)

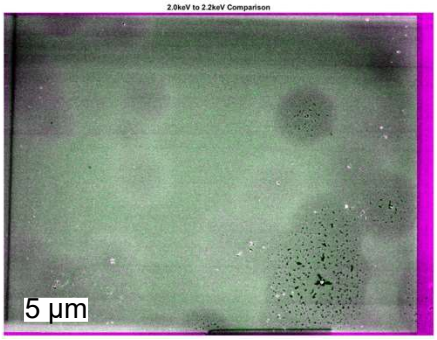

(b)

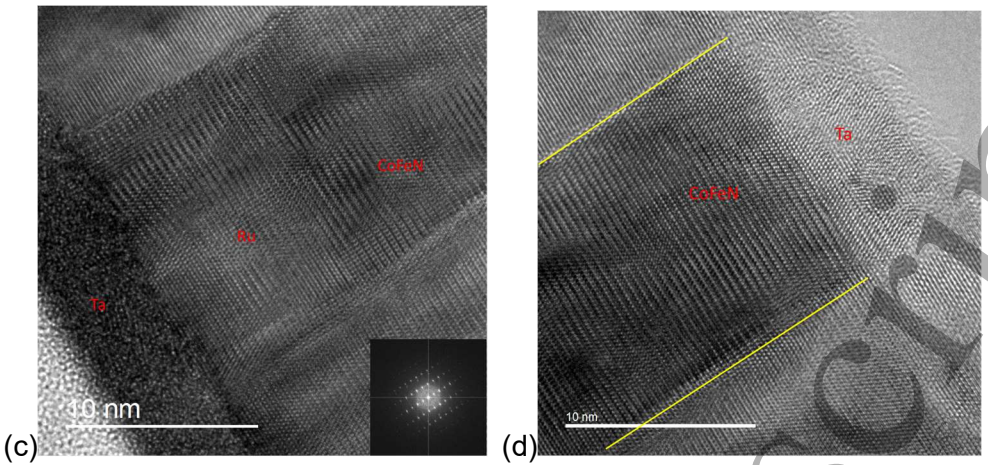

(c) (d)

Fig. 7 SEM images of a Si/SiO_2//Ta/Ru/CoFe:N/Ta multilayer subtracted between the electron-beam acceleration of (a) 0.6 and 0.7 keV to highlight the CoFe:N/Ta interface and (b) 2.0 and 2.2 keV to highlight the Ru/CoFe:N interface. (c) and (d) Cross-sectional TEM image of the interfaces with the same multilayered structure including a selected area electron diffraction pattern as an inset in (c).

Cross-sectional high resolution TEM images of the interfaces are shown in Figs. 7(c) and (d). The grain boundaries in CoFe:N can now be identified clearly and are labeled in Fig. 7(d). Inspecting the cross-sectional TEM images it is found that the CoFe:N grains depend on the grain structures of the Ru seed layer and affect the structure of the Ta capping layer above, *i.e.*, columnar growth.

In summary, the defects observed in Fig. 7(a) can be due to the uneven distribution of N in the CoFe:N layer. Such defects are more obvious at the interface between CoFeN/Ta rather than CoFeN/Ru. This may due to the introduced N gas that is fixed by, but not crystallised within, the CoFe alloy in areas of high concentration. This allows for the formation of TaN during the sputtering of the Ta capping layer. Whilst TEM analysis provided excellent confirmation of the grains and columnar growth within the structure, the SEM analysis done in this case indicated the same thing with a much shorter analysis time. The power of this non-destructive technique is the ability to quickly ascertain information across large areas. This quick analysis allows more lengthy techniques to become more effective as samples have already been screened. The information from the non-destructive SEM imaging, once corroborated by a traditional technique, provides excellent information on the quality of interfaces across the wafer or device.

3.3. *In-situ* imaging

For the precise evaluation of current distributions at a junction interface, an *in-situ*

setup has been developed in SEM (see Fig. 8). This comes at a time when SEM techniques are also being developed to image dopant contrast in semiconductors .[17]. The fabricated device is secured and bonded to a chip carrier to allow for easy connections. To make secure electrical connections and to stabilise the chip carrier a reusable holder was three-dimensionally (3D) printed. This holder allows non-solder connections to be made, by compressing the wires onto the contact pads once the lid is tightened. This also acts to hold the chip carrier in place and provides a large surface to mount the setup to the SEM stage. These connections are connected, via a custom feedthrough, to a current source (Keithley, 2400 SourceMeter) for the application of current and a voltage meter (Keithley, 2400 SourceMeter) for voltage measurements in a conventional four-terminal configuration. Additionally, these connections act to ground the sample, reducing charge build up greatly. This *in-situ* setup allows us to mimic the junction operation whilst observing the sample in an SEM. It also allows the precise determination of the junction area whilst operating and makes it possible to investigate the breakdown processes of a junction.

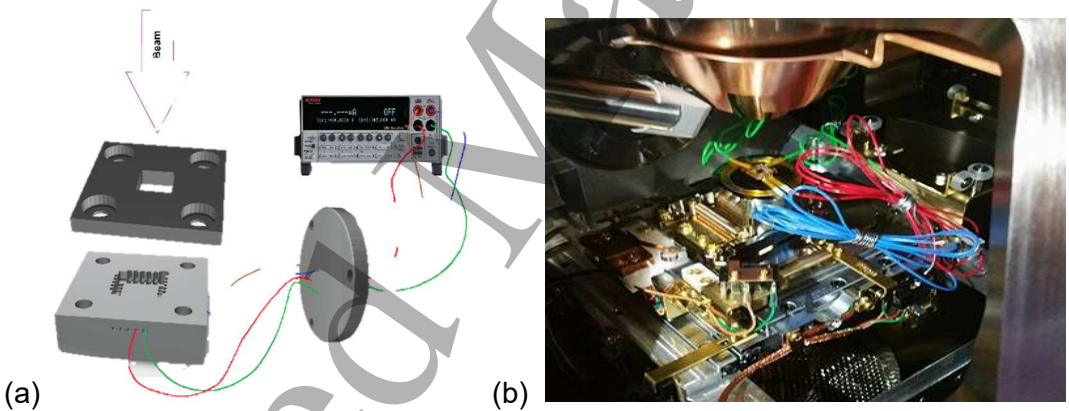

(a) (b)

Fig. 8 In-situ imaging stage developed for four-terminal measurements. (a) is the schematic of the setup and (b) is the system during development

As an example, an Fe/GaAs(001) lateral spin-valve device has been imaged using the *in-situ* setup developed as above. The epitaxial Fe films were grown using ultrahigh vacuum molecular beam epitaxy (UHV-MBE) with the optimised process as reported previously [18]. The films were patterned into a lateral spin-valve using a combination of electron-beam lithography, photolithography, Ar-ion milling and chemical etching. The width of the Fe wires is 4, 1 and 20 μm for the injector, first detector and second detector, respectively. The size of the GaAs mesa is 2 μm thick.

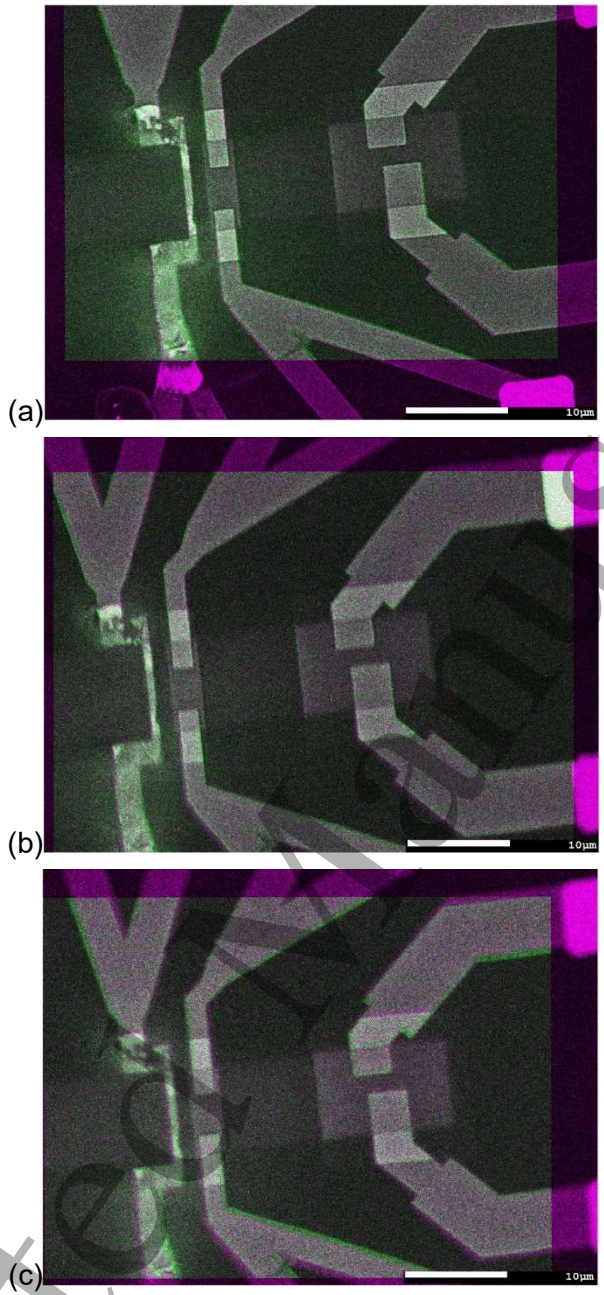

Fig. 9 In-situ SEM images of Fe/GaAs lateral spin-valves subtracted between the electron-beam acceleration of 2.5 and 3.0 keV to highlight the interfaces. These images are measured under the current applications of (a) 0.25, (b) 200 and (c) 400 μA.

A non-local geometry has been used to introduce spin-polarised electrons into the GaAs mesa at elevated current between 0.25 and 400 μA. As shown in Fig. 9, the left spin injector is shown with bright colour, indicating the Fe/GaAs interfaces underneath the injector is activated. In Fig. 9(a), there are some distributions in the contrast of the injector, especially three ~1-μm-diameter grey dots are seen in the 4-μm-wide injector.

These dots generate less BSEs than the surrounding area, revealing that the current density in these dots are smaller than that in the surrounding are. This fact indicates that the current distributions are not uniform under the current application of 0.25 μA. By increasing the current to 200 μA as shown in Fig. 9(b), only one grey dot is observed in the centre of the injector. Increasing the current further to 400 μA almost removes the dots, indicating that the current distribution is almost uniform, as shown in Fig. 9(c). This demonstrates that this subtraction method can visualise electron charge concentrations and the corresponding effective junction area active for transport.

4. Summary

The non-destructive method we developed by combining Monte Carlo electron flight simulations and decelerated electron-beam imaging can be a very powerful tool to characterise buried interfaces in nanoelectronic devices, especially MRAM. The characterised images are fed back to device fabrication processes for their improvement and optimisation. *In-situ* imaging further allows us to correlate the non-destructive images with their electron transport properties, which is ideal as a QA tool. Our imaging method therefore proves its great potential for further improvement of device performance.

Acknowledgements

This work is partially supported by JSPS-EPSRC Core-to-core programme (EP/M02458X/1) and JST CREST (JPMJCR17J5). The authors thank financial and technical support by JEOL UK to develop the non-destructive imaging.

References

[1] T. Endoh, H. Koike, S. Ikeda, T. Hanyu, and H. Ohno, “An Overview of Nonvolatile Emerging Memories— Spintronics for Working Memories,” *IEEE J. Emerg. Sel. Top. Circuits Syst.*, vol. 6, no. 2, pp. 109–119, Jun. 2016.

[2] S. Bhatti, R. Sbiaa, A. Hirohata, H. Ohno, S. Fukami, and S. N. Piramanayagam, “Spintronics based random access memory: a review ⇑,” *Mater. Today d*, vol. 20, no. 9, 2017.

[3] D. B. Williams and C. B. Carter, *Transmission Electron Microscopy: A Textbook for Materials Science*. Plenum Press, 1996.

[4] A. Hirohata, “Method of imaging defects using a scanning electron microscope,” GB1522137.7, 2019.

[5] A. Hirohata, Y. Yamamoto, B. A. Murphy, and A. J. Vick, “Non-destructive imaging

of buried electronic interfaces using a decelerated scanning electron beam," *Nat. Commun.*, vol. 7, p. 12701, 2016.

[6] J. Goldstein *et al.*, *Scanning Electron Microscopy and X-ray Microanalysis: Third Edition*. Springer US, 2013.

[7] P. W. Hawkes, *Electron optics and electron microscopy*. Taylor and Francis, 1972.

[8] T. Mulvey and M. J. Wallington, "Electron lenses," *Reports Prog. Phys.*, vol. 36, no. 4, pp. 347–421, Apr. 1973.

[9] L. Reimer, "Elements of a Transmission Electron Microscope," in *Transmission Electron Microscopy Physics of Image Formation and Microanalysis*, Springer-Verlag Berlin Heidelberg, 1993, pp. 86–135.

[10] P. Hovington, D. Drouin, R. Gauvin, D. C. Joy, and N. Evans, "CASINO: A new monte Carlo code in C language for electron beam interactions-part III: Stopping power at low energies," *Scanning*, vol. 19, pp. 29–35, 1997.

[11] D. Drouin, A. R. Couture, D. Joly, X. Tastet, V. Aimez, and R. Gauvin, "CASINO V2.42 - A fast and easy-to-use modeling tool for scanning electron microscopy and microanalysis users," *Scanning*, vol. 29, no. 3, pp. 92–101, 2007.

[12] N. F. Mott and H. S. W. Massey, *The Theory of Atomic Collisions*, Third Edit. Oxford: Clarendon Press, 1965.

[13] D. C. Joy and S. Luo, "An empirical stopping power relationship for low-energy electrons," *Scanning*, vol. 11, no. 4, pp. 176–180, Jan. 1989.

[14] H. Bethe, "Zur Theorie des Durchgangs schneller Korpuskularstrahlen durch Materie," *Ann. Phys.*, vol. 397, no. 3, pp. 325–400, Jan. 1930.

[15] K. Kanaya and S. Okayama, "Penetration and energy-loss theory of electrons in solid targets," *J. Phys. D. Appl. Phys.*, vol. 5, no. 1, p. 308, Jan. 1972.

[16] E. Jackson, M. Sun, T. Kubota, K. Takanashi, and A. Hirohata, "Chemical and structural analysis on magnetic tunnel junctions using a decelerated scanning electron beam," *Sci. Rep.*, vol. 8, no. 1, p. 7585, 2018.

[17] L. Frank, M. Hovorka, M. M. El-Gomati, I. Müllerová, F. Mika, and E. Mikmeková, "Acquisition of the dopant contrast in semiconductors with slow electrons," *J. Electron Spectros. Relat. Phenomena*, 2019.

[18] L. R. Fleet *et al.*, "Correlating the interface structure to spin injection in abrupt Fe/GaAs(001) films," *Phys. Rev. B*, vol. 87, no. 2, p. 024401, Jan. 2013.